J. Fluid Mech. (1977), *vol.* 83, *part* 3, *pp.* 509–527
Printed in Great Britain

Laminar flow in a square duct of strong curvature

By J. A. C. HUMPHREY, A. M. K. TAYLOR AND J. H. WHITELAW

Department of Mechanical Engineering,
Imperial College, London

(Received 24 February 1977 and in revised form 11 May 1977)

Calculated values of the three velocity components and measured values of the longitudinal component are reported for the flow of water in a 90° bend of 40 × 40 mm cross-section; the bend had a mean radius of 92 mm and was located downstream of a 1·8 m and upstream of a 1·2 m straight section. The experiments were carried out at a Reynolds number, based on the hydraulic diameter and bulk velocity, of 790 (corresponding to a Dean number of 368). Flow visualization was used to identify qualitatively the characteristics of the flow and laser-Doppler anemometry to quantify the velocity field. The results confirm and quantify that the location of maximum velocity moves from the centre of the duct towards the outer wall and, in the 90° plane, is located around 85% of the duct width from the inner wall. Secondary velocities up to 65% of the bulk longitudinal velocity were calculated and small regions of recirculation, close to the outer corners of the duct and in the upstream region, were also observed.

The calculated results were obtained by solving the Navier–Stokes equations in cylindrical co-ordinates. They are shown to exhibit the same trends as the experiments and to be in reasonable quantitative agreement even though the number of node points used to discretize the flow for the finite-difference solution of the differential equations was limited by available computer time and storage. The region of recirculation observed experimentally is confirmed by the calculations. The magnitude of the various terms in the equations is examined to determine the extent to which the details of the flow can be represented by reduced forms of the Navier–Stokes equations. The implications of the use of so-called 'partially parabolic' equations and of potential- and rotational-flow analysis of an ideal fluid are quantified.

1. Introductory remarks

Considerable attention has been devoted to the study of the flow in rectangular ducts and stems from the frequent use in engineering practice of non-circular duct flows of various forms. The turbulent flow in a rectangular duct exhibits the same stress-driven secondary flows as are found in other non-circular ducts and provides a convenient simple geometric shape for detailed examination. In recent years, for example, experimental investigations have been reported by Brundrett & Baines (1964), Gessner & Jones (1965), Launder & Ying (1972) and Melling & Whitelaw (1976) and computational investigations by Launder & Ying (1973) and Tatchell (1975); the latter have made use of the experimental information to guide the development of their solution procedures and particularly of the associated turbulence models.

In the case of bend flows, which are a natural extension of straight duct flows, a similar linking of experimental and computational investigations is desirable but has been forthcoming in only a limited way. Relevant computational investigations have, for example, been reported by Pratap & Spalding (1975) and Patankar, Pratap & Spalding (1975) for turbulent flows and by Austin & Seader (1973), Cheng, Lin & Ou (1976) and Joseph, Smith & Allen (1975) for laminar flows, but related experiments have been confined largely to wall measurements and have limited the extent to which the solution procedures can be appraised.

The present investigation has been motivated by a need to provide a better understanding of the flow in alternator-cooling passages and represents an early step in a long-term research programme. It is concerned with the low Reynolds number flow in a bend in a long rectangular duct. The dimensions of the duct and the radius of the bend are scaled versions of those found in alternators and a low Reynolds number has been chosen partly to allow the features of this geometric arrangement to be investigated without the complication of turbulence and partly to facilitate the development and validation of the numerical method. A previous preliminary examination of turbulent flow in the same bend (Humphrey & Whitelaw 1976) had shown that the turbulence was essentially frozen through the bend and that the pressure-driven secondary flows were much larger than the stress-driven secondary flows. Thus laminar-type equations, with appropriate eddy-viscosity formulations, may prove to be useful in turbulent bend flows and, to some extent, potential-flow and rotational-flow analysis of a perfect fluid may also be of value.

The experimental part of the present investigation made use of flow visualization, by dye traces, and laser-Doppler anemometry. The dye traces provided a visual and qualitative impression of the flow patterns and guided the choice of locations at which detailed velocity measurements were obtained. The anemometer allowed measurements of the local values of the longitudinal velocity components with precision better than that which could be expected from the solution method: these results quantify the velocity characteristics of the flow at six planes including those at the inlet and outlet.

The calculation procedure is based on the numerical solution of finite-difference representations of the Navier–Stokes equations in cylindrical co-ordinates. It was developed from that previously reported by Gosman & Pun (1973) and appropriate to the solution of two-dimensional elliptic equations; only the essential features are reported here and the reader is referred to Humphrey (1977) for detailed information. In general, it is shown that the calculated results are in good agreement with the measurements even though the number of grid nodes is restricted by available computer time and storage. All trends are correctly represented and the quantitative agreement is good. The detailed results allow the magnitude of the various convective, diffusion and source terms to be examined throughout the flow to determine their influence and so allow an assessment of the validity of solutions of reduced equations, which can be achieved with equal numerical precision and greater economy.

The flow configuration and experimental features are described in the next section, which is followed by presentation and discussion of the measured results. The essential features of the solution procedure are described in § 4 and the results presented and discussed, in relation to the measurements, in the final section.

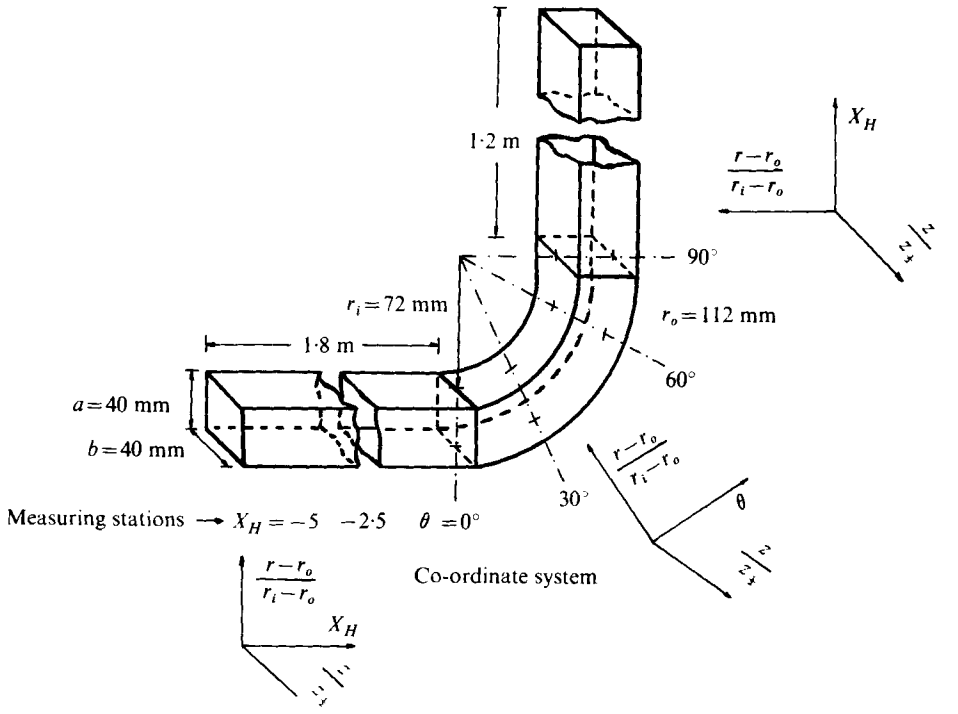

FIGURE 1. Flow configuration and co-ordinate system.

2. Flow configuration, instrumentation and procedures

The flow configuration is a 90° bend of mean radius 92 mm attached to the end of the 1·8 m rectangular channel previously described by Melling & Whitelaw (1976). It was manufactured from 20 mm thick Perspex with a cross-section of

$$40 \pm 0{\cdot}1 \times 40 \pm 0{\cdot}1 \text{ mm};$$

the curved surfaces were machined from solid Perspex and have radii of $72 \pm 0{\cdot}1$ mm and $112 \pm 0{\cdot}1$ mm. The bend was located in the vertical plane with a 1·2 m length of straight duct of the same cross-section attached to its downstream end. The inlet contraction to the 1·8 m duct and the associated constant-head tank and pipework were otherwise identical to those of Melling & Whitelaw.

Flow-visualization tests were carried out with a neutrally buoyant dye injected at various positions in the duct through a 1 mm external diameter probe which was inserted through specially arranged holes and through several pressure tappings located along the side and outer-radius walls of the bend. The streamline nature of the flow at a Reynolds number, based on the bulk velocity V_c ($1{\cdot}98 \times 10^{-2}$ m/s) and hydraulic diameter d ($4{\cdot}0 \times 10^{-2}$ m), of 790 was demonstrated by these traces and confirmed by the negligible fluctuations measured with the laser-Doppler anemometer. The Dean number of the flow was $De \equiv Re(\frac{1}{2}d/R_c)^{\frac{1}{2}} = 368$, where R_c is the mean radius of curvature.

The anemometer was similar to that used by Melling & Whitelaw and discussed by

Durst, Melling & Whitelaw (1976) although the mechanical design of the bend precluded measurements of the z component of velocity (see figure 1). It comprised a 5 mW helium–neon laser, an optical unit of the type described by Durst & Whitelaw (1971), a light collection arrangement, an EMI 9558 B photomultiplier and a frequency-tracking demodulator (DISA 55L20).

The mean velocity was read out on a Solartron digital voltmeter and the r.m.s. fluctuations, which proved to be negligible, observed on a DISA true r.m.s. meter. The angle between the transmitted light beams was 14·5° and, together with the forward-scatter on-line collection system, resulted in a control volume calculated to be 1·47 mm in length and 187 μm in diameter: the effective dimensions were reduced by the discrimination level of the frequency-tracking demodulator. Particles were not added to the water, which contained sufficient natural contaminant to provide an almost continuous Doppler signal on the monitoring oscilloscope. The combined effect of transit-time, gradient and noise broadening was evaluated and had negligible influence on the measured mean velocity, which had an estimated precision of around $\pm$ 0·5 % of the bulk velocity.

3. Measured results

Half-profiles of the longitudinal velocity component normalized by the bulk velocity are presented in figure 2 for the six measuring stations indicated on figure 1 and were obtained as follows. At all radial positions shown, and additional ones at 60 and 90°, measurements of the longitudinal velocity components were taken over the whole depth of the duct to check that the flow was symmetrical. Since this indeed was the case, to within experimental precision, the data on either side of the symmetry line were averaged to produce the profiles shown. Although figure 2 presents only five radial positions per measuring station seven or more profiles were taken at each station with, for example, 11 and 13 profiles for the 60° station.

The profiles measured at $X_H = -5$ (hydraulic diameters) correspond to a fully developed square-duct flow. Between $X_H = -5$ and $\theta = 0$, an acceleration can be detected in the flow at a value of $(r-r_o)/(r_i-r_o)$ of 0·7 and is due to the favourable longitudinal pressure gradient at the inner-radius wall. Conversely, because of an adverse pressure gradient at the outer-radius wall a small deceleration occurs at values of $(r-r_o)/(r_i-r_o)$ of around 0·1 between $X_H = -2{\cdot}5$ and $\theta = 0$.

In the bend itself, the profiles demonstrate the general movement of the fluid away from the inner-radius wall and towards the outer-radius wall. This progressive movement is accompanied by a secondary motion directed towards the side walls along the outer-radius wall and towards the symmetry plane along the inner-radius wall and is particularly pronounced at the two furthest downstream stations. At the inner-radius wall, between the 30 and 90° stations a large deceleration is observed in the flow which corresponds to the region of adverse longitudinal pressure gradient. A corresponding acceleration, due to a favourable gradient, occurs at the outer-radius wall and is intensified by the transfer of high-speed fluid by the secondary motion from the duct centre towards the outer-radius wall.

Corresponding contours of constant longitudinal velocity, again normalized with the bulk velocity, are shown in figures 3 (*c*, ii) and (*d*, ii) for the 60 and 90° positions. These were obtained from the measured data by least-squares polynomial regression.

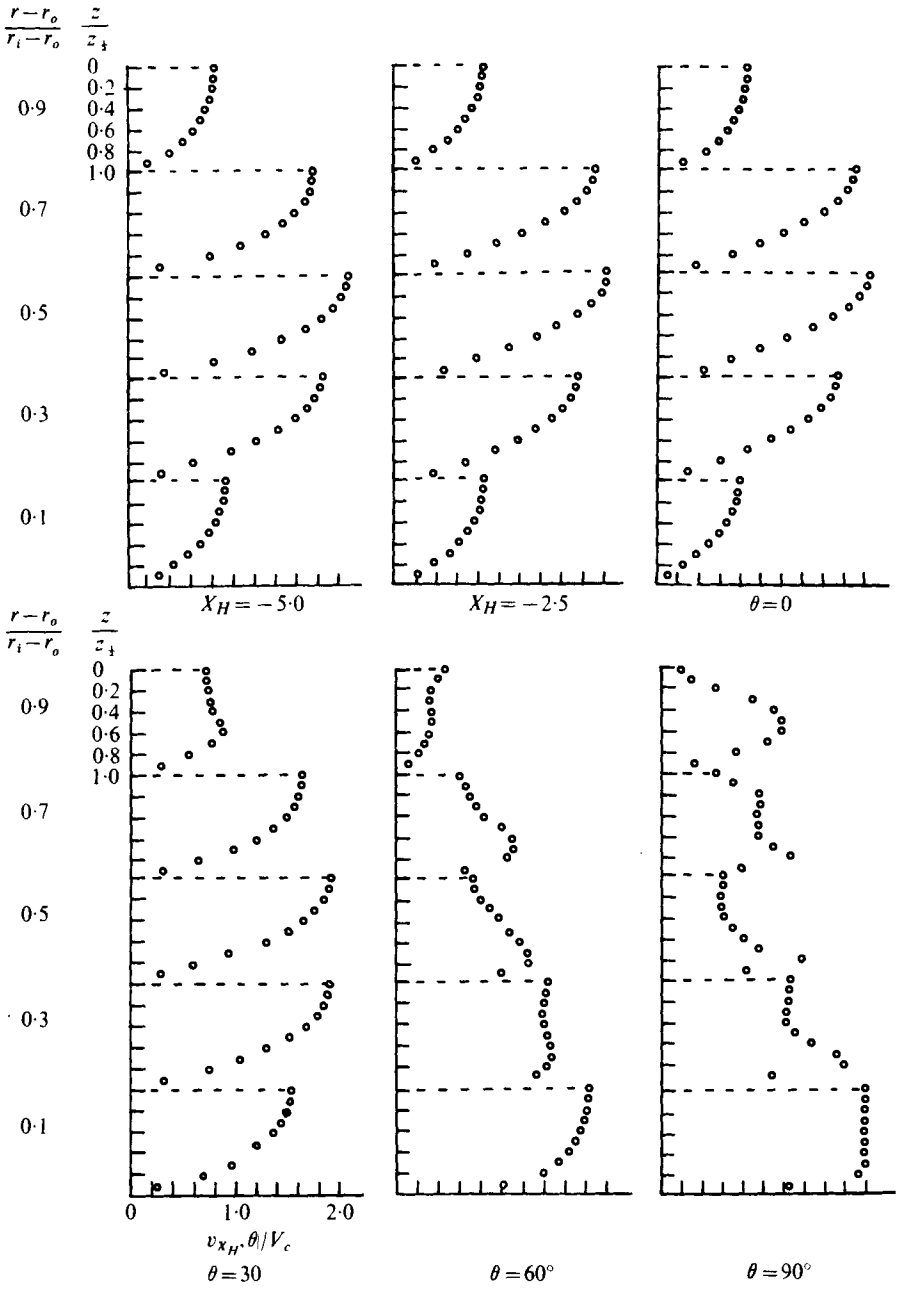

FIGURE 2. Representative measurements of the longitudinal velocity component.

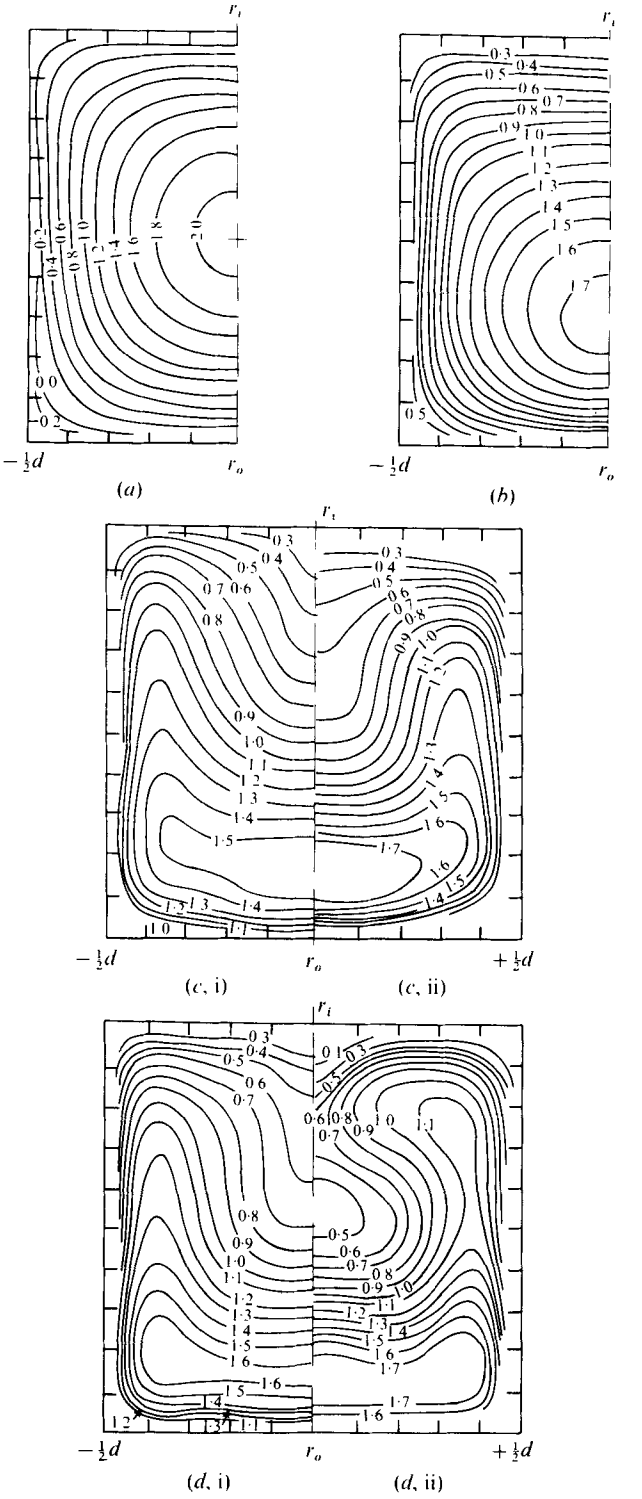

FIGURE 3. Measured and computed velocity (v_θ/V_c) contours in the bend flow: (*a*) 0° (calculated), (*b*) 30° (calculated), (*c*, i) 60° (calculated), (*c*, ii) 60° (measured), (*d*, i) 90° (calculated), (*d*, ii) 90° (measured).

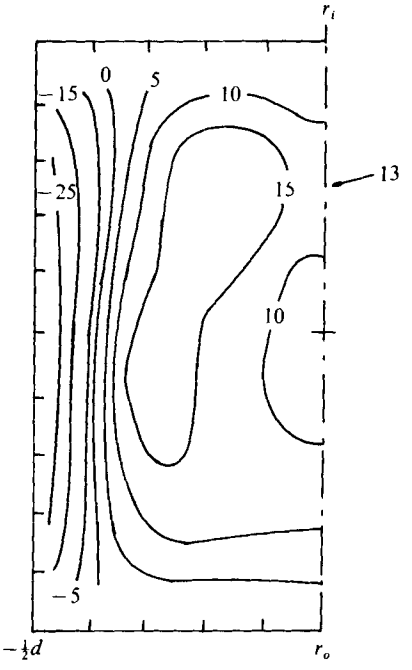

FIGURE 4. Calculated contours of radial velocity component $[(v_r/V_c) \times 10^2]$ in 90° plane.

Tests verified that possible bias introduced by the regression procedure was negligible in comparison with the curvature existing in the measured flow profiles.

Figures 3(*a*), (*b*), (*c*, i) and (*d*, i) show calculated results and will be discussed later. The consequences of the strong secondary velocities are particularly noticeable at the two downstream stations, where the higher-velocity regions have been moved substantially towards the outer-radius wall and the side walls.

A further indication of the secondary velocities can be deduced from figure 4, which presents contours of the calculated radial velocity component at the 90° station. The maximum symmetry-plane value of the radial velocity was $0{\cdot}13V_c$ and corresponds to the location identified on the figure. It should be noted that the secondary flows stem from the pressure-field imbalance; the maximum radial velocity noted by Humphrey & Whitelaw (1976) for the corresponding turbulent flow was $0{\cdot}28V_c$ at $z/z_{\frac{1}{2}} = 0$ and $(r-r_o)/(r_i-r_o) = 0{\cdot}5$ and stemmed from the pressure field rather than normal stresses.

Values of the longitudinal velocity component were obtained in greater detail than that indicated by figure 2 in the vicinity of the symmetry plane of the duct and adjacent to the inner- and outer-radius walls. Thus the slope of the near-wall linear velocity gradient was deduced and allowed the calculation of the friction coefficients shown in figure 5(*a*); calculated values of C_f are also shown on this figure and calculated values of the corresponding overall pressure coefficient on figure 5(*b*) and will be discussed later. The measurements extend from the near-linear upstream region into the bend, where the values on the outer-radius wall rise by a factor of more than three to a maximum at around the 60° station; on the inner-radius wall, C_f increases over

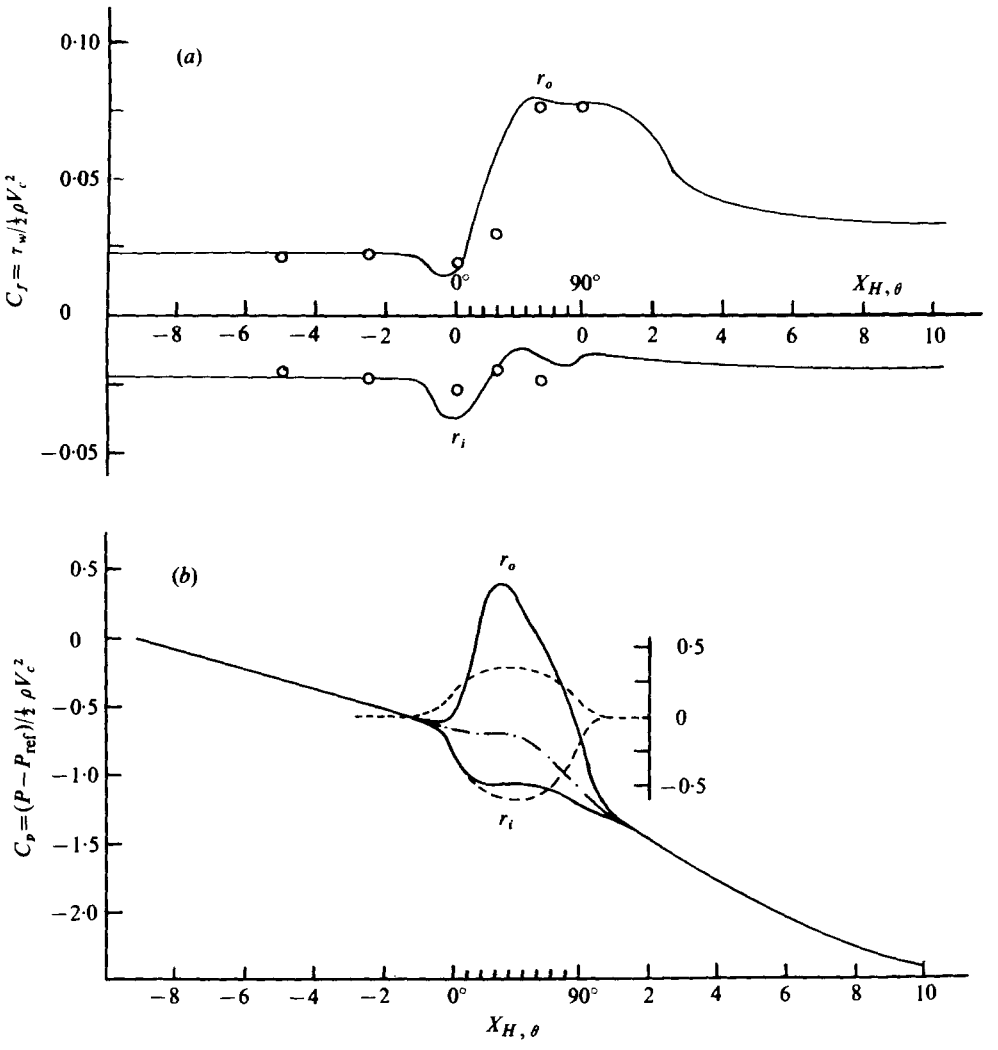

FIGURES 5 (*a*, *b*). For caption see facing page.

the first 30° then falls to a minimum at around 60° before rising again to a maximum at the exit plane.

A similar pattern of C_f distributions might be expected at locations away from the symmetry plane but figure 6 (plate 1) suggests that this may be complicated by a region of recirculating flow which the dye traces revealed and subsequently the calculations confirmed. This small region of recirculation exists on the outer-radius wall, between 0 and 25° approximately and close to the side walls. The figure shows that the dye trace curves in the $\pm z$ directions and is turned against the direction of the bulk flow for a small but finite distance. It is likely that, in this wall region, the value of $\frac{1}{2}C_f$ will become locally zero along two stagnation lines and negative in the intervening small area.

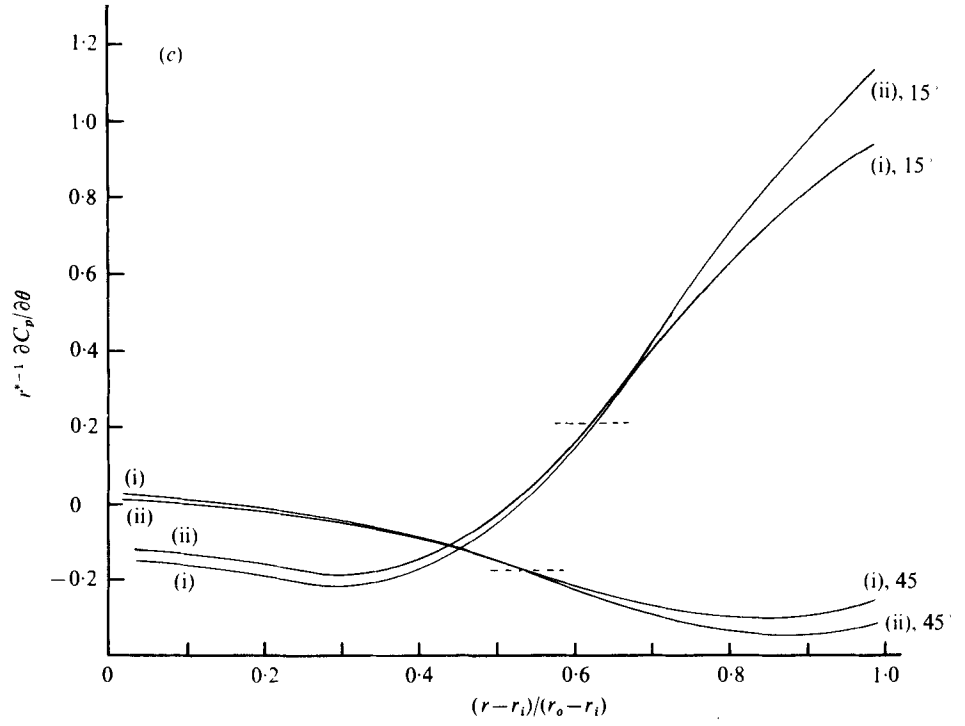

FIGURE 5. (*a*) Measured (circles) and computed friction coefficients at the centre-line of the inside and outside curved walls of the bend. (*b*) Computed pressure coefficients at the centre-line: —·—, computed average; – – –, potential-flow solution. (*c*) Computed radial variation of longitudinal pressure gradient at the 15 and 45° planes at the centre-line: (i) $r^* = (r-r_i)/(r_o-r_i)$; (ii) $r^* = R_c/(r_o-r_i)$; – – –, plane average.

4. Equations, boundary conditions and numerical solution procedure

The momentum equations in differential form appropriate to the present three-dimensional, steady, incompressible laminar flow may be written in cylindrical co-ordinates as

$$\rho\left[v_r\frac{\partial v_r}{\partial r}+\frac{v_\theta}{r}\frac{\partial v_r}{\partial\theta}+v_z\frac{\partial v_r}{\partial z}-\frac{v_\theta^2}{r}\right]=-\frac{\partial P}{\partial r}+\mu\left[\nabla^2 v_r-\frac{v_r}{r^2}-\frac{2}{r^2}\frac{\partial v_\theta}{\partial\theta}\right], \tag{1}$$

$$\rho\left[v_r\frac{\partial v_\theta}{\partial r}+\frac{v_\theta}{r}\frac{\partial v_\theta}{\partial\theta}+v_z\frac{\partial v_\theta}{\partial z}+\frac{v_r v_\theta}{r}\right]=-\frac{1}{r}\frac{\partial P}{\partial\theta}+\mu\left[\nabla^2 v_\theta+\frac{2}{r^2}\frac{\partial v_r}{\partial\theta}-\frac{v_\theta}{r^2}\right], \tag{2}$$

$$\rho\left[v_r\frac{\partial v_z}{\partial r}+\frac{v_\theta}{r}\frac{\partial v_z}{\partial\theta}+v_z\frac{\partial v_z}{\partial z}\right]=-\frac{\partial P}{\partial z}+\mu\nabla^2 v_z \tag{3}$$

and

$$\nabla^2=\frac{\partial^2}{\partial r^2}+\frac{1}{r}\frac{\partial}{\partial r}+\frac{1}{r^2}\frac{\partial^2}{\partial\theta^2}+\frac{\partial^2}{\partial z^2}. \tag{4}$$

The mass conservation equation is given by

$$\frac{\partial v_r}{\partial r}+\frac{1}{r}\frac{\partial v_\theta}{\partial\theta}+\frac{\partial v_z}{\partial z}+\frac{v_r}{r}=0. \tag{5}$$

Where the radius of curvature is infinite, i.e. in the upstream and downstream straight sections of the duct, the momentum and conservation equations reduce to the familiar rectangular form

$$\rho v_j \frac{\partial v_i}{\partial x_j} = -\frac{\partial P}{\partial x_i} + \mu \frac{\partial^2 v_i}{\partial x_j^2} \tag{6}$$

and

$$\partial v_j / \partial x_j = 0. \tag{7}$$

It is required to solve (1)–(3) and (5) together with the following boundary conditions: in the initial plane (all z and r at $\theta = X_H = -10$),

$$v_\theta = \text{developed duct flow}, \quad v_z = v_r = 0;$$

on the side walls (all θ or X_H),

$$v_\theta = v_r = v_z = 0 \quad \text{at} \quad z = \pm z_{\frac{1}{2}}, \quad r = r_o, r_i;$$

in the symmetry plane (all r and θ or X_H at $z = 0$),

$$v_z = 0, \quad \partial v_\theta / \partial z = \partial v_r / \partial z = 0;$$

in the exit plane (all z and r at $\theta = X_H = \pm 10$),

$$\partial v_\theta / \partial \theta = \partial v_z / \partial \theta = \partial v_r / \partial \theta = 0$$

with overall continuity imposed.

Finite-difference equations are formulated by integration of (1)–(3) and (5) over volume elements or 'cells' discretizing the flow domain. The main dependent variables are the velocity components and pressure and these are calculated on a number of staggered, interconnected grids, each of which is associated with a particular variable: the general form of the finite-difference equation is

$$\phi_P \sum_{i=1}^{6} A_i = \sum_{i=1}^{6} A_i \phi_i + S_0, \tag{8}$$

where ϕ_P is the variable (velocity component or pressure) solved for at a position P in the flow; the A_i coefficients are found at the six cell surfaces and represent the combined effects of convection and diffusion on the balance of ϕ, and the S_0 term contains the contributions arising from pressure, centrifugal and Coriolis forces and other non-rectangular diffusion terms arising in cylindrical co-ordinates. A more detailed account of the derivation of the finite-difference equation in curvilinear co-ordinates is given by Humphrey (1977).

The solution algorithm is similar to that used by Gosman & Pun (1973) and Patankar & Spalding (1971) and is based on the earlier work of, for example, Harlow & Welch (1965), Chorin (1968) and Amsden & Harlow (1970). It is different, however, in that it solves fully elliptic forms of the Navier–Stokes equation in three dimensions and can be readily adapted for arbitrary curvilinear orthogonal co-ordinates from a knowledge of the co-ordinate scale factors.

The algorithm involves solving the three momentum equations and the continuity equation in finite-difference form by means of a cyclic series of predict and correct operations. In this way, the velocities are first calculated from the momentum equations for a guessed pressure field, which is calculated in turn, then the velocities are adjusted such that continuity is satisfied. The actual method of solution is based

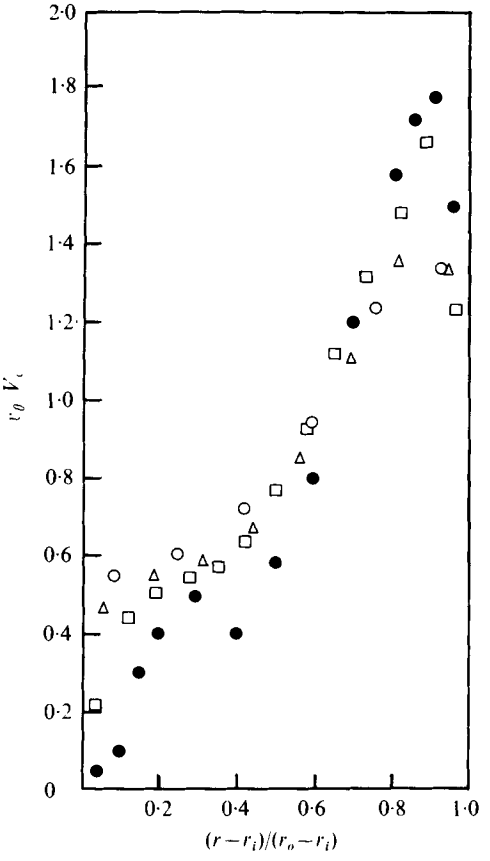

FIGURE 7. Influence of number of nodes in cross-stream planes on the centre-line ($z/z_{\frac{1}{2}} = 0$) velocity profile at the 90° position. ○, 8 × 8; △, 10 × 10; □, 10 × 15; ●, experimental.

on the standard tridiagonal matrix algorithm (TDMA) as described, for example, by Patankar & Spalding (1971).

The stages in a calculation cycle are as follows:

(1) The guessed pressure field (or the field from a previous iteration) P^* is substituted into forms of the momentum equation which are linearized, i.e. with coefficients and source terms evaluated from the previous cycle and held constant throughout the subsequent cycle.

(2) The momentum equations are then solved to yield a field of intermediate velocity components v_i^*, which do not necessarily satisfy continuity.

(3) A pressure correction field P' is obtained by bringing the intermediate velocity values v_i^* into conformity with the continuity equation and a corrected pressure field given by $P = P^* + P'$ is obtained.

(4) The intermediate velocity field $\mathbf{v}^*$ is updated by means of the P' field found in step 3 to obtain the more accurate velocity field $\mathbf{v}$.

(5) Steps 1–4 are repeated until the convergence criterion is satisfied.

To ensure sufficient node points to represent the strongly curved flow, the first duct, the bend and the second duct were treated separately with overlapping boundaries. During a calculation sequence on any one part the intermediate results for the

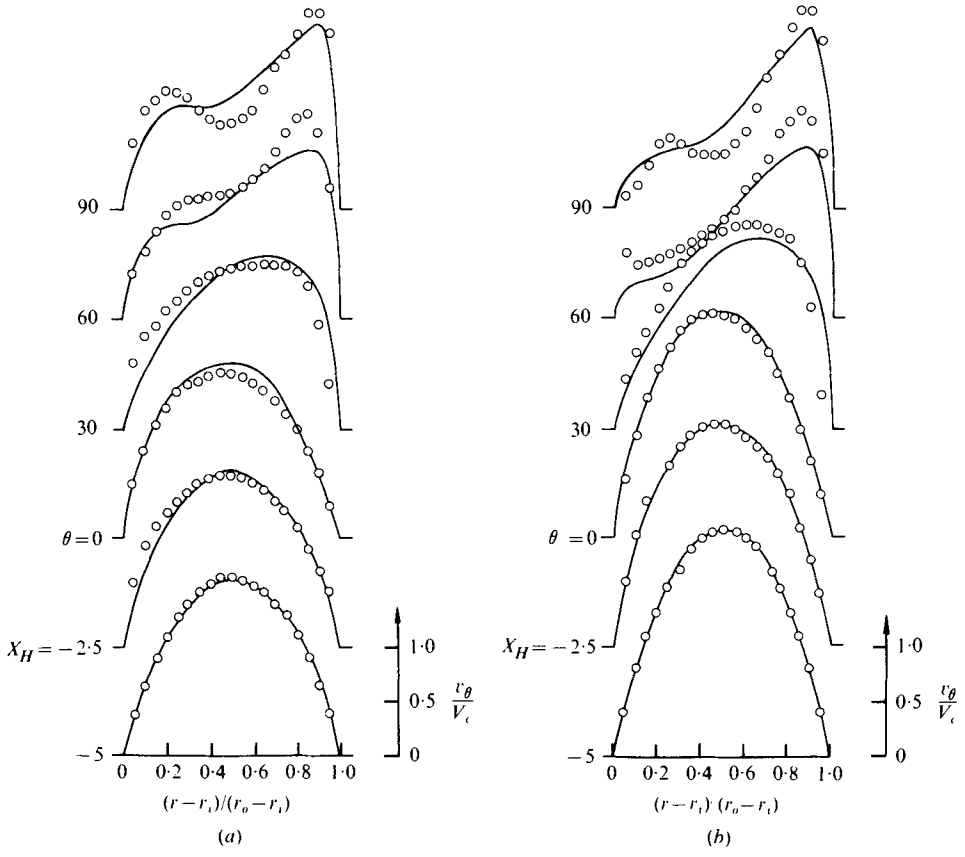

FIGURE 8. Comparison between measured (circles) and computed velocity profiles: (*a*) $z/z_{\frac{1}{2}} = 0{\cdot}5$, (*b*) $z/z_{\frac{1}{2}} = 0$.

other two were stored on disc, the time required for a converged solution being approximately 80 min of CDC 6600 CP time for a $10 \times 15 \times 60$ grid mesh. The convergence criterion consisted of ensuring that the largest of the normalized residuals in any one of the four conservation equations should be less than 10^{-3}. While a finer grid than the one used would have been desirable it would have resulted in prohibitive storage and computing time costs.

Extensive numerical testing of the solution procedure was carried out and has been documented by Humphrey (1977). An example directly relevant to the present flow is shown on figure 7, where the influence of the number of cross-stream node points is demonstrated for the symmetry-plane profile of longitudinal velocity at the 90° station. These results were obtained with 20 grid planes in the flow direction and in the bend. It is clear that the 10×15 grid (15 lines in the radial direction where gradients are steeper) smooths the peaks indicated by the measurements but that the experimental trends are well represented. It is also clear that a considerably larger number of node points would be required to represent the measured trends significantly more closely. Comparisons, with similar discrepancies, were found at other locations with similarly steep gradients; in other regions of the flow and indeed

throughout the greatest part of the flow, the discrepancies were smaller and usually considerably smaller.

On the basis of tests like those shown on figure 7, the calculated results presented here were obtained with a mesh which corresponded to $10 \times 15 \times 20$ nodes in each of the three parts. The time required for a converged solution is $(I \times E \times S \times N)2 \times 10^{-4}$ s for E equations, S sweeps of the TDMA and I iterations on a grid with N nodes. Subsequent runs for similar geometries, using the pressure field from the present calculations as a first approximation, converged in a much shorter time.

Figure 8 presents calculated profiles of the longitudinal velocity at values of $z/z_{\frac{1}{2}}$ of 0 and 0·5 and allows comparison with the measured values at each of the six measurement stations. The results, in general, confirm the comments of the previous paragraph in relation to the discrepancies between measurement and calculation.

5. Discussion

The results in figure 3, in particular, demonstrate the complexity of the present flow, which stems from the curvature and the associated pressure field. In this figure contour plots of the measured results are given only for 60 and 90°, where sufficient experimental data were obtained to determine them accurately. It is clear from the figure that the mean flow in the entrance plane of the bend has been significantly influenced by the downstream flow. This elliptic influence is confirmed by the magnitude of the radial variation of the longitudinal pressure gradient, as shown in figure 5(*c*) for the 15 and 45° planes. Figure 5(*c*) also shows a very large and unfavourable longitudinal pressure gradient at the outer-radius wall in the 15° plane, which causes the flow reversal predicted and observed between 0 and 25°.

It is interesting to note that the corresponding preliminary turbulent-flow results of Humphrey & Whitelaw (1976) indicated an upstream influence of approximately similar magnitude; in contrast, the normal stresses upstream of and at the 0° plane were similar in magnitude to those in the 45° plane. This suggests that the transport of turbulence energy may be of little significance in this upstream region; the measurements downstream also suggested small turbulence transport. The apparent dominance of the pressure field further suggests that an effective-viscosity hypothesis (in contrast to a Reynolds-stress model) will be adequate for the calculation of developed duct flows of significant curvature.

The calculated distributions of the friction and pressure coefficients (figure 5) demonstrate good agreement with the measured results and with the correlations presented by Ward-Smith (1971). Unlike the pressure distributions, the two distributions of C_f do not converge quickly to the same magnitude. This is due to the residual secondary flows as may be confirmed from figure 9, which presents calculated secondary velocities at six stations. In the 0° plane, the secondary flow is already established with magnitudes up to $0{\cdot}15V_c$; the calculated secondary velocities at $-0{\cdot}30X_H$ had magnitudes up to $0{\cdot}07V_c$ but the vortical pattern did not exist. The secondary velocities attain maximum magnitudes up to $0{\cdot}30V_c$ in the 90° plane with a similar, but rather more confined, vortex pattern. Further downstream, the magnitude of the secondary flows decays but is still apparent at $X_H = 10$, showing that straight duct flow (without secondary motion) has not been re-established. This result is supported by the differences in slope of the pressure-coefficient curves in figure

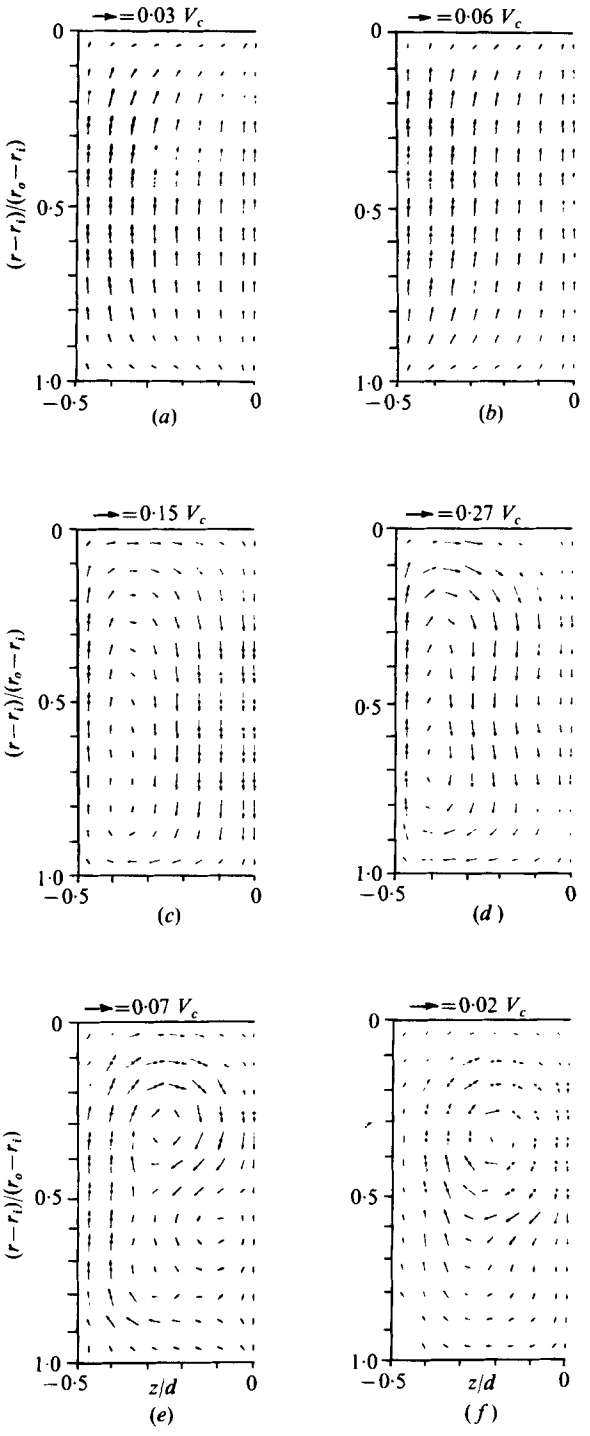

FIGURE 9. Computed vector plots of secondary velocity: (*a*) $-0{\cdot}90d$, (*b*) $-0{\cdot}30d$, (*c*) 0°, (*d*) 90°, (*e*) $2{\cdot}80d$, (*f*) $10d$.

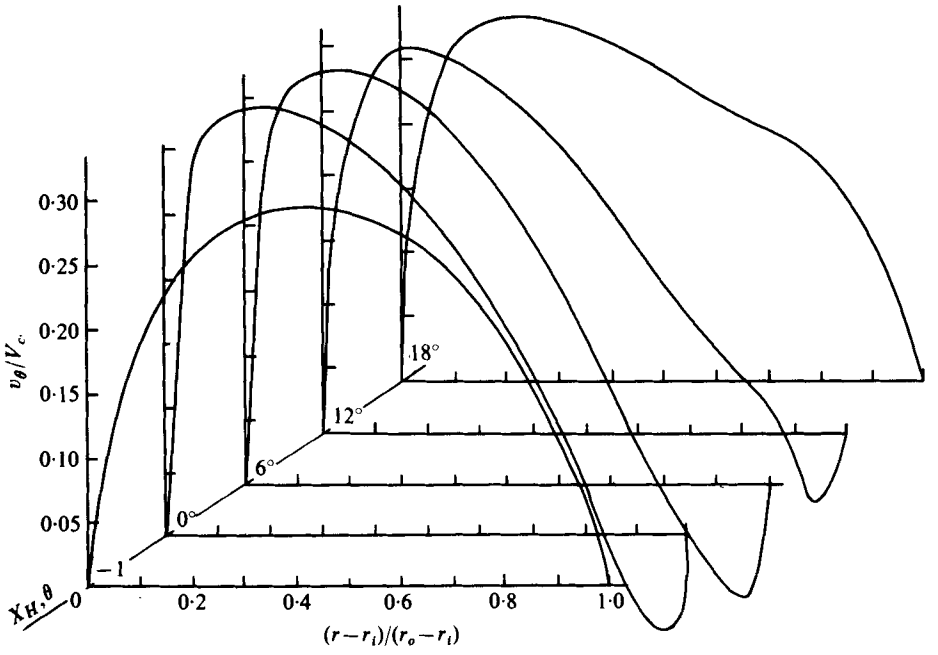

FIGURE 10. Computed velocity distribution in the recirculating region of the bend flow; $z/z_{\frac{1}{2}} = 0{\cdot}94$.

5 (*b*) but does not invalidate the boundary conditions assumed for the exit plane since changes in the $\theta = X_H$ direction were indeed small. The apparent mechanism of the breakdown of the vortex structure is indicated by the results at $X_H = 2{\cdot}80$ and 10 (figure 9).

In Ito's (1960) theoretical analysis of fully developed flow in a curved square duct, based upon an expansion in increasing powers of the Dean number, the secondary-flow streamlines had their centre at approximately $z/z_{\frac{1}{2}} = \pm 0{\cdot}45$ and

$$(r-r_o)/(r_i-r_o) = 0{\cdot}5.$$

In contrast, at the 90° plane in the present work the secondary motion circulates about $z/z_{\frac{1}{2}} = \pm 0{\cdot}38$ and $(r-r_o)/(r_i-r_o) \simeq 0{\cdot}70$. However, Ito's analysis is valid for mildly curved flows while the measurements and calculations here correspond to a *De* of 368 (a relatively highly curved flow). It is therefore likely that the differences are due more to the strong effects of the secondary motion than to not having fully developed flow at 90°.

The secondary flow velocities calculated in the 0° plane were probably slightly influenced by the downstream recirculation, whose magnitude is quantified further on figure 10 in the z plane where the calculations suggested it to be most extensive. The maximum negative velocity is less than 0·27 of the maximum positive velocity at the same x and z locations and the maximum radial distance over which it exists is less than 0·20 of the width but it extends in the longitudinal direction from upstream of the entrance plane to beyond the 12° location. Nevertheless, its influence is local and cannot be expected to have a major influence on previously presented profiles.

The present calculations are expensive in computer time and are still imperfect. It

is important to ask, therefore, what reduction in precision may be associated with the solution of partially parabolic and ideal-fluid flow equations. Reduced forms of the equations of § 4 may be obtained with the following assumptions:

$\partial^2/\partial\theta^2 = 0$,	partially parabolic;
$\partial^2/\partial\theta^2 = 0$ and $\partial P/\partial\theta = f(\theta)$ with f prescribed,	parabolic;
$\nu = 0$ and finite vorticity,	ideal, rotational;
$\nu = 0$ and zero vorticity,	ideal, irrotational or potential.

The solution of the potential-flow equations is comparatively simple and very inexpensive. It cannot, of course, lead to values of the skin-friction drag nor predict secondary flows but, as shown, for example, by Huang, Robertson & McPherson (1967) and Ward-Smith (1971), useful calculations of the pressure coefficient can be obtained. A pressure distribution corresponding to the present geometry and to the tabulated potential-flow results of Ward-Smith is shown on figure 5(*b*) and is in some agreement with the present results although the steep gradients and large maximum at the outer-radius wall are not represented.

Rotational-flow equations have been shown, for example by Hawthorne (1951) and Squire & Winter (1951), to represent flows with curvature provided that the bend angle and radius ratio are small and the aspect ratio large. The secondary flows, for example, have the correct trends provided that the side walls are far apart; the quantitative discrepancies can, however, be considerable even for the large aspect ratio situation. Again, the influence of skin-friction drag is not represented and the pressure distributions are similar to those of the irrotational flow. In turbulent bend flow, in contrast, potential flow does represent the pressure distribution of bends with aspect ratio equal to one or larger with precision satisfactory for engineering purposes, provided that the radius ratio is not too severe; see Ward-Smith.

The calculated results indicated that at the 45° plane the longitudinal diffusion is usually less than 0·05 of the total diffusion for the present flow; in addition, it is usually less than 0·001 of the longitudinal convection. Thus the neglect of longitudinal diffusion should lead to approximately correct results for substantial regions of the flow. The representation of the flow by parabolic equations is, however, unlikely to lead to reasonable results in view of the substantial radial variations in the longitudinal pressure gradient indicated by figure 5(*c*). Partially parabolic equations are likely to be more successful although they cannot represent the region of the flow influenced by the separation of figures 6 and 10; in the 9° plane, for example, near the recirculation zone the ratio of longitudinal to total diffusion is 0·5 and of longitudinal diffusion to longitudinal convection 0·9.

The main difficulty inherent in the use of these reduced-form equations is the need for *a priori* information that, for example, there is no region of separated flow or significant radial pressure distribution. There is, therefore, a need to provide solutions based on the equations of this paper for a range of aspect and radius ratios. A small sample is provided in figure 11.

Three aspect ratios ($b/a = \frac{1}{3}$, 1 and 3) and four radius ratios ($R_c/d = 0{\cdot}75$, 1·5, 2·3 and 4) are represented by the five diagrams of figure 11, which correspond to the 90° plane of bends with flow Reynolds numbers lower than that of the present investigation. In general, the results show a reduction of the intensity of the secondary flow with a change in aspect ratio from unity and an enhancement of the secondary flow,

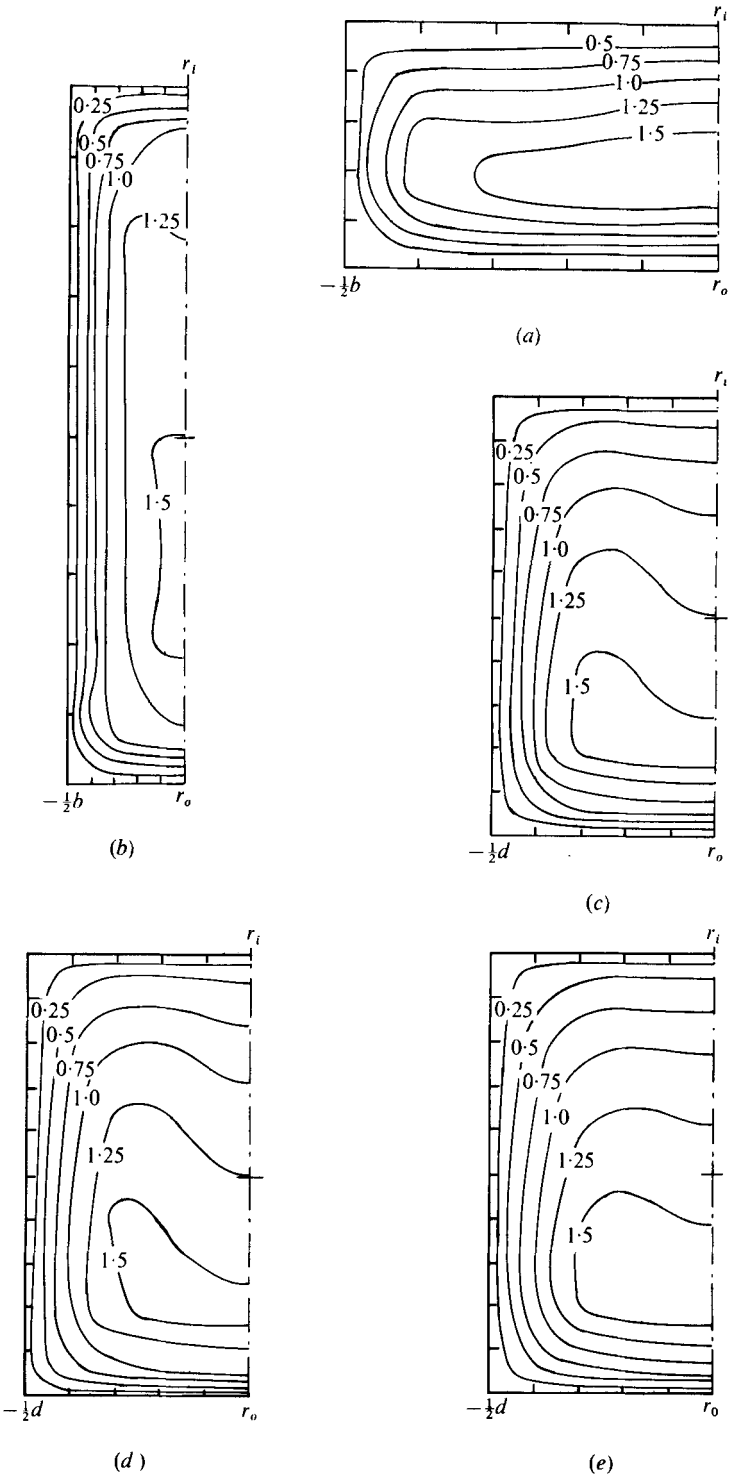

FIGURE 11. Computed velocity (v_θ/V_c) contours in the 90° plane: (*a*) $De = 86$, $b/a = 3$, $R_c/d = 1{\cdot}5$; (*b*) $De = 86$, $b/a = 1/3$, $R_c/d = 1{\cdot}5$; (*c*) $De = 70$, $b/a = 1$, $R_c/d = 2{\cdot}3$; (*d*) $De = 122$, $b/a = 1$, $R_c/d = 0{\cdot}75$; (*e*) $De = 53$, $b/a = 1$, $R_c/d = 4$.

with a displacement of the maximum velocity towards the outer-radius wall, with decreasing radius of curvature. Of these configurations, (*b*) and (*e*) indicated two additional counter-rotating vortices near the outer-radius wall, similar to that in figure 9(*e*) and those previously calculated by Cheng *et al.* (1975) and Joseph *et al.* (1975) for fully developed laminar flow in a helical coil. All flows indicated significant radial pressure gradients but, contrary to the $Re = 790$ case, recirculation in the longitudinal direction was not observed, probably owing to the lower Dean numbers and corresponding weaker secondary motion.

The above results, together with related calculations, suggest that regions of recirculation exist for bend flows with $De > 125$. These regions occur in the initial 25° and near the outside corners of the bends and can significantly influence the surrounding flow. Preliminary results suggest that much stronger curvature is required to induce separation in turbulent flows. Once the existence of a region of separation has been established, economical computation of the flow can be achieved by an appropriate combination of elliptic and partially parabolic equations.

Financial support was made available by the Science Research Council in the form of grant B/RG/7801 and a Studentship (A. M. K. T). We are glad to have this opportunity to acknowledge this support and to record our thanks.

REFERENCES

AHMED, S. & BRUNDRETT, E. 1971*a* Turbulent flow in non-circular ducts. Part I. Mean flow properties in the developing region of a square duct. *Int. J. Heat Mass Transfer* **14**, 365.

AHMED, S. & BRUNDRETT, E. 1971*b* Characteristic lengths for non-circular ducts. *Int. J. Heat Mass Transfer* **14**, 157.

AMSDEN, A. A. & HARLOW, F. H. 1970 The SMAC method. *Los Alamos Sci. Lab. Rep.* LA-4370.

AUSTIN, L. R. & SEADER, J. D. 1973 Fully developed viscous flow in coiled circular pipes. *A.I.Ch.E. J.* **19**, 85.

BERGELES, G. 1976 Three-dimensional discrete-hole cooling processes. An experimental and numerical study. Ph.D. thesis, University of London.

BRUNDRETT, E. & BAINES, W. D. 1964 The production and diffusion of vorticity in duct flow. *J. Fluid Mech.* **19**, 375.

CHENG, K. G., LIN, R. C. & OU, J. W. 1976 Fully developed laminar flow in curved rectangular channels. *A.S.M.E. J. Fluids Engng* **198**, 41.

CHORIN, A. J. 1968 Numerical solution of the Navier–Stokes equations. *Math. Comp.* **22**, 745.

DURST, F. & WHITELAW, J. H. 1971 Integrated optical units for laser anemometry. *J. Phys.* E **4**, 804.

DURST, F., MELLING, A. & WHITELAW, J. H. 1976 *Principles and Practices of Laser-Doppler Anemometry*. Academic Press.

GESSNER, F. B. 1964 Turbulence and mean flow characteristics of fully-developed flow in rectangular channels. Ph.D. thesis, Purdue University.

GESSNER, F. B. & JONES, J. B. 1965 On some aspects of fully developed turbulent flow in rectangular channels. *J. Fluid Mech.* **23**, 689.

GOSMAN, A. D. & PUN, W. M. 1973 Calculation of recirculating flows. *Imperial College Mech. Engng Dept. Rep.*

HARLOW, F. H. & WELCH, J. E. 1965 Numerical calculation of time-dependent viscous incompressible flow of fluid with free surface. *Phys. Fluids* **8**, 2182.

HAWTHORNE, W. R. 1951 Secondary circulation in fluid flow. *Proc. Roy. Soc.* A **206**, 374.

HUANG, W. H., ROBERTSON, J. M. & MCPHERSON, M. B. 1967 Some analytical results for plane 90 degree bend flow. *J. Hydraul. Div., Proc. A.S.C.E.* HY**6**, 169.

HUMPHREY, J. A. C. 1977 Flow in ducts with curvature and roughness. Ph.D. thesis, University of London.

HUMPHREY, J. A. C. & WHITELAW, J. H. 1976 Measurements in curved flows. *Proc. SQUID Conf. Internal Flows, Airlie House.*

ITO, H. 1960 Pressure losses in smooth pipe bends. *Trans. A.S.M.E.* D **82**, 131.

JOSEPH, B., SMITH, E. P. & ALLEN, R. J. 1975 Numerical treatment of laminar flow in helically coiled tubes of square cross section 1. Stationary helically coiled tubes *A.I.Ch.E. J.* **21**, 965.

LAUNDER, B. E. & YING, W. M. 1972 Secondary flows in ducts of square cross-section. *J. Fluid Mech.* **54**, 289.

LAUNDER, B. E. & YING, W. M. 1973 Prediction of flow and heat transfer in ducts of square cross section. *Heat Fluid Flow* **3**, 115.

MELLING, A. & WHITELAW, J. H. 1976 Turbulent flow in a rectangular duct. *J. Fluid Mech.* **78**, 289.

PATANKAR, S. V., PRATAP, V. S. & SPALDING, D. B. 1975 Prediction of turbulent flow in curved pipes. *J. Fluid Mech.* **67**, 583.

PATANKAR, S. V. & SPALDING, D. B. 1971 A calculation procedure for heat, mass and momentum transfer in three-dimensional parabolic flows. *Int. J. Heat Mass Transfer* **15**, 1787.

PRATAP, V. S. & SPALDING, D. B. 1975 Numerical computations of the flow in curved ducts. *Aero. Quart.* **26**, 219.

SQUIRE, H. B. & WINTER, K. G. 1951 The secondary flow in a cascade of airfoils in a non-uniform stream. *J. Aero. Sci.* **18**, 271.

TATCHELL, D. G. 1975 Convection processes in confined three dimensional boundary layers. Ph.D. thesis, University of London.

WARD-SMITH, A. J. 1971 *Pressure Losses in Ducted Flows.* Butterworths.

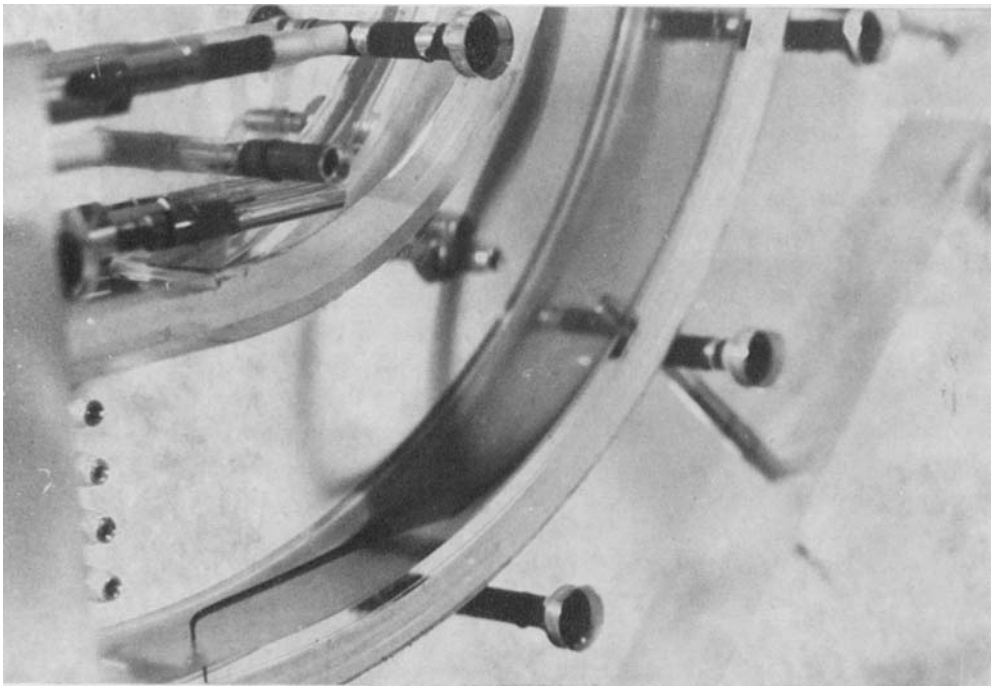

FIGURE 6. Visualization of the recirculating region at the outside curved wall and side walls. Dye injected at 0° plane through pressure tapping located in the centre of the outer-radius wall.